The Propagation of Tsunami-Generated Acoustic–Gravity Waves in the Atmosphere

YUE WU, STEFAN G. LLEWELLYN SMITH, AND JAMES W. ROTTMAN

Department of Mechanical and Aerospace Engineering, University of California, San Diego, La Jolla, California

DAVE BROUTMAN

Computational Physics, Inc., Springfield, Virginia

JEAN-BERNARD H. MINSTER

Scripps Institution of Oceanography, University of California, San Diego, La Jolla, California

(Manuscript received 26 August 2015, in final form 26 April 2016)

ABSTRACT

Tsunami-generated acoustic–gravity waves have been observed to propagate in the atmosphere up to the ionosphere, where they have an impact on the total electron content. The authors simulate numerically the propagation of two-dimensional linear acoustic–gravity waves in an atmosphere with vertically varying stratification and horizontal background winds. The authors' goal is to compare the difference in how much energy reaches the lower ionosphere up to an altitude of 180 km, where the atmosphere is assumed to be anelastic or fully compressible. The authors consider three specific atmospheric cases: a uniformly stratified atmosphere without winds, an idealized case with a wind jet, and a realistic case with an atmospheric profile corresponding to the 2004 Sumatra tsunami. Results show that for the last two cases, the number and height of turning points are different for the anelastic and compressible assumptions, and the net result is that compressibility enhances the total transmission of energy through the whole atmosphere.

1. Introduction

Tsunami-generated acoustic–gravity waves propagate through the atmosphere up to the ionosphere, where their impact on the total electron content can be detected by ionospheric sounding techniques using the global positioning system (GPS). Peltier and Hines (1976) first suggested that this ionospheric response could be used for purposes of tsunami warning. The development of high-density, real-time GPS networks has allowed observational evidence of tsunamis: Artru et al. (2005) observed from the GEONET network in Japan a short-scale ionospheric perturbation produced by the tsunami associated with a magnitude 8.2 earthquake in Peru. This was the first observation of ionospheric response to a tsunami. Then Liu et al. (2006), Rolland et al. (2010), Galvan et al. (2011, 2012), and Coïsson et al. (2015) also presented observational evidence of ionospheric signatures of tsunamis. Numerical (i.e., Occhipinti et al. 2006, 2008, 2011; Hickey et al. 2009, 2010; Mai and Kiang 2009) examined the vertical propagation of tsunami-generated internal waves through the atmosphere. Ding et al. (2003) investigated the influence of background winds on the propagation of atmospheric gravity waves using a ray-tracing method that includes attenuation. Broutman et al. (2014, hereafter BED) simulated the propagation of tsunami-generated gravity waves through a realistic atmosphere with vertically varying stratification and horizontal background winds in the anelastic approximation.

Compressibility is an important feature of the real atmosphere, as are the background winds. Wei et al. (2015) examined the propagation of acoustic–gravity waves in an atmosphere with piecewise background winds.

Corresponding author address: Yue Wu, Department of Mechanical and Aerospace Engineering, Jacobs School of Engineering, University of California, San Diego, 9500 Gilman Dr., La Jolla, CA 92093-0411.
E-mail: wuyue@ucsd.edu

DOI: 10.1175/JAS-D-15-0255.1

© 2016 American Meteorological Society

There are two branches of internal atmospheric waves: the gravity branch, which is dominated by the restoring buoyancy force of the stratified atmosphere, has a relatively lower frequency; the acoustic branch, which is dominated by compression and expansion of the air, has a relatively higher frequency (Lighthill 2001).

Waves in the acoustic branch propagate rapidly. A disturbance at the sea surface will reach the ionosphere in approximately 10 min, whereas waves in the gravity branch will reach in a few hours. However, that is not the effect that is being considered in this paper, which simulates the steady propagation in the tsunami reference frame of two-dimensional linear acoustic–gravity waves through a compressible atmosphere with background wind up to the lower ionosphere at 180 km. We stop at 180 km because above this altitude other effects need to be considered, such as nonneutral effects due to ionization, nonlinearity due to the exponentially increasing velocity with altitude, and increasing viscosity.

The contribution of this work is to generalize the algorithm of BED to include compressibility of the atmosphere. Section 2 describes the model formulation, where we obtain the governing equations for a rescaled vertical velocity that includes a factor accounting for the altitude-dependent density and the Doppler effect considering sound speed in a moving background, as well as a vertical wavenumber depending on buoyancy frequency, density scale height, sound speed, and background wind velocity. In section 3 we investigate three different wind profiles: a uniformly stratified atmosphere without winds, an idealized wind jet, and a realistic atmosphere representative of the 2004 Sumatra tsunami. Results show that compressibility has a nonnegligible effect on the number and height of turning points, as well as on the wave transmission and reflection. Conclusions are presented in section 4.

2. Formulation

We consider a tsunami to be a group of shallow-water surface waves that travel across the ocean basin at a phase speed $c = \sqrt{gH_s}$, where g is the gravitational acceleration and H_s is the mean ocean depth.

In the tsunami reference frame, the horizontal background wind velocity, assumed steady and altitude dependent, is specified as

$$U(z) = U_a(z) - c, \tag{1}$$

where $U_a(z)$ is the wind velocity in a reference frame fixed to Earth.

The governing equations for an adiabatic compressible atmosphere are

$$\frac{D\mathbf{v}}{Dt} = -\frac{1}{\rho}\nabla p + \mathbf{g}, \tag{2}$$

$$\frac{D\rho}{Dt} = -\rho\nabla\cdot\mathbf{v}, \quad \text{and} \tag{3}$$

$$\frac{Dp}{Dt} = c_s^2\frac{D\rho}{Dt}, \tag{4}$$

where $\mathbf{v}$ is the velocity vector, t is time, ρ is density, p is pressure, $\mathbf{g}$ is the vector of the gravitational acceleration, and c_s is the speed of sound.

In two dimensions, after linearizing

$$\rho_0\frac{\partial u_1}{\partial t} + \rho_0 U\frac{\partial u_1}{\partial x} + \rho_0 w_1\frac{\partial U}{\partial z} = -\frac{\partial p_1}{\partial x}, \tag{5}$$

$$\rho_0\frac{\partial w_1}{\partial t} + \rho_0 U\frac{\partial w_1}{\partial x} = -\frac{\partial p_1}{\partial z} - \rho_1 g, \tag{6}$$

$$\frac{\partial \rho_1}{\partial t} + U\frac{\partial \rho_1}{\partial x} + w_1\frac{\partial \rho_0}{\partial z} = -\rho_0\left(\frac{\partial u_1}{\partial x} + \frac{\partial w_1}{\partial z}\right), \quad \text{and} \tag{7}$$

$$\frac{\partial p_1}{\partial t} + U\frac{\partial p_1}{\partial x} + w_1\frac{\partial p_0}{\partial z} = c_s^2\left(\frac{\partial \rho_1}{\partial t} + U\frac{\partial \rho_1}{\partial x} + w_1\frac{\partial \rho_0}{\partial z}\right), \tag{8}$$

where u_1 and w_1 are the perturbations of horizontal and vertical velocities due to waves, respectively; ρ_0 and p_0 are the background density and pressure, respectively; and ρ_1 and p_1 are the perturbations of density and pressure, respectively. The anelastic equations are obtained by setting the sound speed to infinity, such that only the right-hand side of (8) dominates, as in Smith (1979).

The background density and pressure satisfy the hydrostatic equation

$$\frac{dp_0}{dz} = -\rho_0 g. \tag{9}$$

This problem can be formulated in the wavenumber domain in terms of $\tilde{w}_1$, which is the Fourier transform of the perturbed vertical velocity w_1 and satisfies a second-order ordinary differential equation in z. The tilde denotes the Fourier transform in the horizontal. It is convenient to introduce a new variable $\tilde{w}$ that includes a factor accounting for the altitude-dependent density and the Doppler effect D:

$$\tilde{w} = \sqrt{\frac{\rho_0(z)}{\rho_0(0)}}\,\frac{\tilde{w}_1}{D} \quad \text{and} \tag{10}$$

$$D = \sqrt{1 - \frac{U^2}{c_s^2}}, \tag{11}$$

such that (10) satisfies the Taylor–Goldstein equation expressed as

$$\tilde{w}_{zz} + m^2\tilde{w} = 0, \tag{12}$$

where the subscripts z and zz denote the first and second derivative in z, respectively.

The square of the vertical wavenumber m^2 is a function of buoyancy frequency N, U, density scale height H (expressed by S), the horizontal wavenumber k, and c_s (expressed by D):

$$m^2 = \frac{N^2}{U^2} + \frac{SU_z}{U} - \frac{U_{zz}}{U} + \frac{S_z}{2} - \frac{S^2}{4} - k^2D^2 - \frac{SD_z}{D} + \frac{D_{zz}}{D} - \frac{2D_z^2}{D^2} + \frac{2gD_z}{U^2D} + \frac{2U_zD_z}{UD}, \tag{13}$$

$$N^2 = -g\frac{\rho_{0z}}{\rho_0} - \frac{g^2}{c_s^2}, \quad \text{and} \tag{14}$$

$$S = \frac{1}{H} = -\frac{\rho_{0z}}{\rho_0}. \tag{15}$$

The first five terms in m^2 are the anelastic terms, as in (2.23) of Smith (1979). The sixth term is a compressible modification of the anelastic term $-k^2$ and reduces to its anelastic form as $c_s \to \infty$. The last five terms are the additional compressible terms: they are added to the anelastic terms in the compressible case but vanish in the anelastic case when $c_s \to \infty$. In an isothermal atmosphere at rest, (13) reduces to the dispersion relations of Hines (1960).

The lower boundary condition is expressed as

$$\tilde{W}(k) = \frac{1}{2\pi}\int_{-\infty}^{\infty} W(x)e^{-ikx}\,dx = ikU_0\tilde{h}(k), \tag{16}$$

where $\tilde{W}(k)$ is the Fourier transform of the tsunami vertical velocity $W(x)$, U_0 is the wind velocity at the sea surface, and $\tilde{h}(k)$ is the Fourier transform of the tsunami vertical displacement $h(x)$.

To obtain the numerical solution for the rescaled vertical velocity $\tilde{w}$, we first set up a two-dimensional grid in the x–z plane, where the x axis coincides with the average sea surface at $z = 0$ and the z axis points up. The horizontal scale is 3000 km with grid spacing 15 km and the vertical coordinate reaches up to 180 km with grid spacing 500 m. We use Fourier components with horizontal wavenumber k linearly distributed in the range from $k_{\max} = 0$ to $k_{\min} = -\pi/(\text{the horizontal grid spacing}) = -2.09 \times 10^{-4}\ \text{m}^{-1}$. In this range, the wavenumber corresponding to the maximum absolute tsunami vertical velocity $|\tilde{W}(k)|$ is $K_0 = 1.55 \times 10^{-5}\ \text{m}^{-1}$. The lower boundary is nonreflecting: downgoing waves reach the lower boundary without being reflected back upward, while the effect of acoustic–gravity waves to the tsunami itself is neglected (Peltier and Hines 1976; Occhipinti et al. 2006; BED).

The upper boundary has a radiation boundary condition, which permits energy to leave the domain but not enter from above. We obtain m^2 for each Fourier component using (13) and select initially propagating waves with $m^2 > 0$ at $z = 0$. We integrate (12) from top to bottom with the radiation upper boundary conditions, then obtain the numerical solutions in the Fourier domain (Broutman et al. 2014).

To separate upgoing and downgoing waves, we write the solution to (12) for each Fourier component in the form of a WKB approximation

$$\tilde{w} = A(k,z)e^{-i\theta} + B(k,z)e^{i\theta}, \tag{17}$$

where θ is the phase function with $m = \theta_z$.

The first derivative of this expression neglecting the z derivative of A and B is

$$\tilde{w}_z = -imA(k,z)e^{-i\theta} + imB(k,z)e^{i\theta} + \ldots. \tag{18}$$

The WKB approximation is valid theoretically when (Fröman and Fröman 2002)

$$\epsilon = \frac{1}{16|m|^6}\left|5\left(\frac{dm^2}{dz}\right)^2 - 4m^2\frac{d^2m^2}{dz^2}\right| \ll 1. \tag{19}$$

We select the positive root of (13) when m is real, so A and B represent the upgoing and downgoing waves, respectively; or we select exponentially decaying waves as $z \to +\infty$ when m is imaginary. Then we calculate the coefficients A and B from the numerical solutions for $\tilde{w}$ and $\tilde{w}_z$ by combining (17) and (18):

$$A(k,z)e^{-i\theta} = \frac{im\tilde{w} - \tilde{w}_z}{2im} \quad \text{and} \tag{20}$$

$$B(k,z)e^{i\theta} = \frac{im\tilde{w} + \tilde{w}_z}{2im}. \tag{21}$$

At the nonreflecting sea surface, tsunami-generated upgoing waves are rescaled to satisfy the lower boundary conditions in (16):

$$A(k, z = 0) = \tilde{W}(k). \tag{22}$$

Finally, we perform the inverse Fourier transform

$$w(x,z) = \int_{-\infty}^{\infty} \tilde{w}(k,z)e^{ikx}\,dk. \tag{23}$$

We plot upgoing and downgoing waves in the spatial domain separately but do not show the solutions in regions with $\epsilon > 1$ when the WKB approximation that we use to separate the upgoing and downgoing waves is not valid.

Transmission and reflection coefficients through the whole atmosphere for each Fourier component are defined as

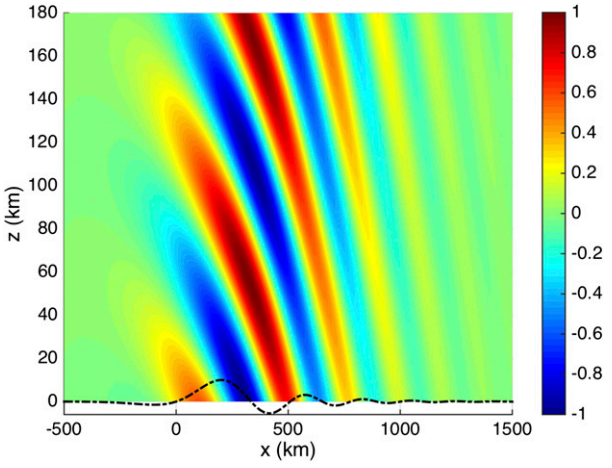

FIG. 1. The normalized vertical velocity w/W_0 with the tsunami vertical displacement $h(x)$ (dashed–dotted line; not to scale) in a uniformly stratified compressible atmosphere without winds.

$$T(k) = \left|\frac{A(k, z_{\max})}{A(k,0)}\right| \left[\frac{m(k, z_{\max})}{m(k,0)}\right]^{1/2} \quad \text{and} \quad (24)$$

$$R(k) = \left|\frac{B(k,0)}{A(k,0)}\right|. \quad (25)$$

Note that a factor of $[m(k, z_{\max})/m(k,0)]^{1/2}$, which is the square root of the ratio of the vertical wavenumber at the upper boundary to that at the sea surface, is included owing to the conservation of wave action instead of wave energy for wave propagation in a moving background (Bretherton and Garrett 1968).

3. Results

During propagation across the Indian Ocean, the Sumatra tsunami had a wavelength of about 400 km, a period of about 20 min, and a maximum vertical displacement of 0.5 m. The Indian Ocean stretches for more than 10 000 km with an average depth of 4 km. Hence, given the dispersion relations for shallow-water gravity waves $c = \sqrt{gH_s}$, we estimate the tsunami phase speed to be approximately 200 m s^{-1}. When the tsunami is approximately midway across the Indian Ocean, we use a representative model profile for the vertical displacement of the sea surface (Peltier and Hines 1976)

$$h(x) = aAi(1 - x')(x'/2)\exp[(2 - x')/2], \quad (26)$$

where Ai is the Airy function, x' is horizontal distance measured in units of 100 km, and a is a coefficient that normalizes the maximum displacement to 0.5 m.

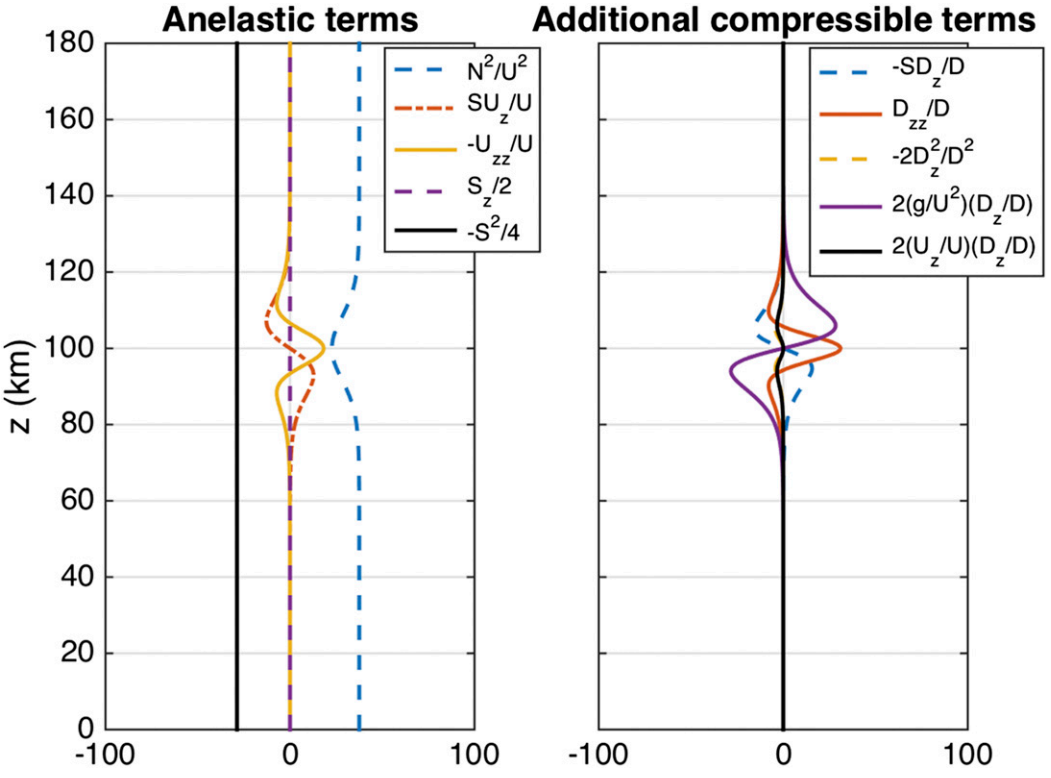

FIG. 2. Terms in the normalized vertical wavenumber m^2/K_0^2.

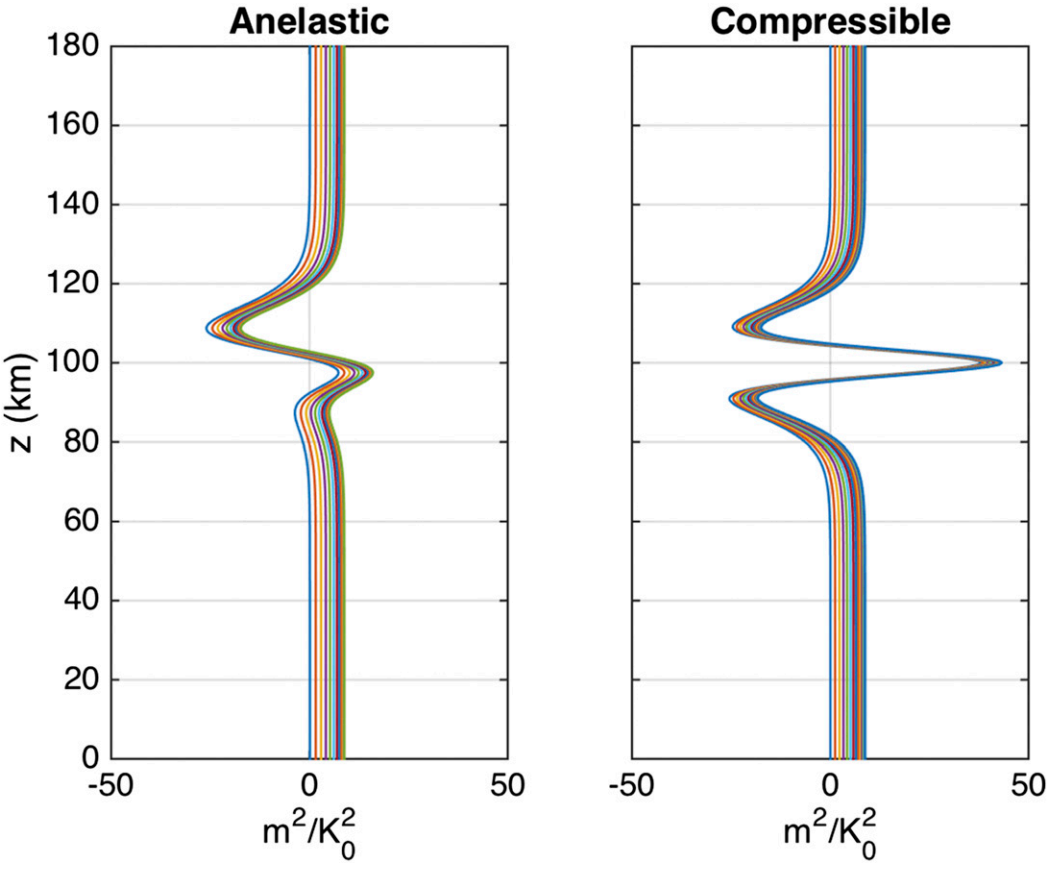

FIG. 3. Profiles of m^2/K_0^2 for every 10 initially propagating waves in the wind jet case.

a. Case 1: Uniformly stratified atmosphere without winds

We simulate wave propagation through a uniformly stratified atmosphere without winds with buoyancy frequency $N = 0.02\,\mathrm{s}^{-1}$ and density scale height $H = 6\,\mathrm{km}$ as in case 1 of BED. Since all parameters are constant in z, terms that contain the z gradient in (13) vanish; thus, (13) becomes

$$m^2 = N^2/U^2 - 1/(4H^2) - k^2D^2. \tag{27}$$

We use $k \in [-2.09 \times 10^{-4}, 0]\,\mathrm{m}^{-1}$ and estimate $N^2/U^2 = 1 \times 10^{-8}\,\mathrm{m}^{-2}$ and $1/(4H^2) = 6.94 \times 10^{-9}\,\mathrm{m}^{-2}$. Note that the term $-k^2D^2$ is a compressible modification of k^2, where $D \in [0, 1]$ and $D = 1$ when anelastic. Hence in the compressible case, we expect more propagating waves since $-k^2D^2 > -k^2$, which allows more waves with smaller k to propagate. We find the numbers of initially propagating waves in the anelastic and compressible cases are 135 and 167, respectively, which verifies our analysis. In Fig. 1 we plot the rescaled vertical velocity w as defined in (10) normalized by the maximum tsunami vertical velocity W_0 in the compressible atmosphere. The vertical structure of wave propagation should be identical to that in the anelastic case: waves propagate upward without being reflected. Compressibility does increase the number of propagating waves, but the difference is not visible in the spatial domain when comparing our Fig. 1 with BED's Fig. 2.

b. Case 2: Idealized wind jet

We now add horizontal wind to the background so that U_a is positive and $c = -200\,\mathrm{m\,s}^{-1}$. We consider the same model profile of a wind jet as BED:

$$U_a = U_0 + U_1\,\mathrm{sech}^2[(z - z_m)/L], \tag{28}$$

with $U_0 = 10\,\mathrm{m\,s}^{-1}$, $U_1 = 60\,\mathrm{m\,s}^{-1}$, $z_m = 100\,\mathrm{km}$, and $L = 10\,\mathrm{km}$. The full width at half maximum (FWHM) of sech^2 is $2\,\ln(1 + \sqrt{2})L$.

Figure 2 is a plot of the anelastic terms and the additional compressible terms except for k^2D^2 in m^2/K_0^2 in the left and right panels, respectively. In the left panel of Fig. 2, we see that N^2/U^2 and $-S^2/4$ are the largest positive and negative anelastic terms at all altitudes,

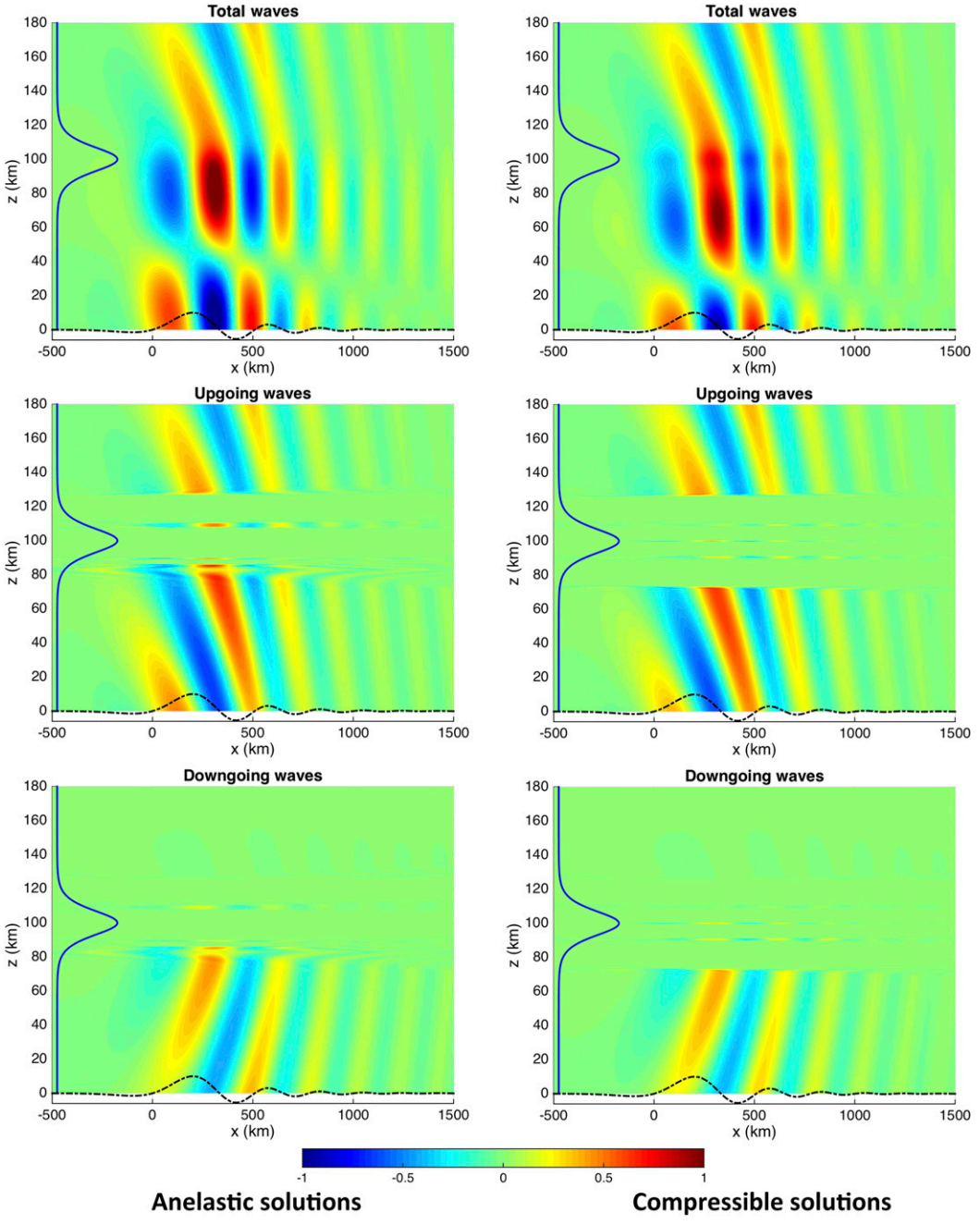

FIG. 4. Cross sections of w/W_0 for the (top) total, (middle) upgoing, and (bottom) downgoing waves with $h(x)$ and the wind velocity $U(z)$ (solid line; not to scale) in the (left) anelastic and (right) compressible cases.

respectively. Note that all terms are symmetric about the jet axis at 100 km except for SU_z/U, which is positive below 100 km and negative above 100 km. In the right panel of Fig. 2, we see that $2(g/U^2)(D_z/D)$ has the maximum variation among all additional compressible terms, and D_{zz}/D has the largest positive value at 100 km. Also note that there are two terms $2(g/U^2)(D_z/D)$ and $-SD_z/D$ that are nonsymmetric. Combining the two panels of Fig. 2, we see that the additional compressible terms have a comparable value to the anelastic terms.

Figure 3 is a plot of m^2/K_0^2 as a function of height for every 10 initially propagating waves with $m^2 > 0$ at $z = 0$ in the anelastic and compressible cases, respectively. Positive m^2 implies propagating waves and negative m^2 implies evanescent waves. The zeros of m^2 indicate turning points. The left panel of Fig. 3 shows m^2/K_0^2 in

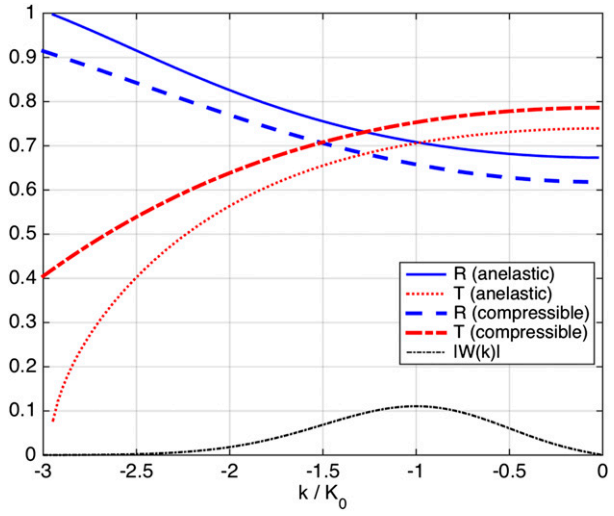

FIG. 5. Transmission $T(k)$, reflection $R(k)$, and the tsunami vertical velocity $|\tilde{W}(k)|$ (not to scale) in the wind jet case.

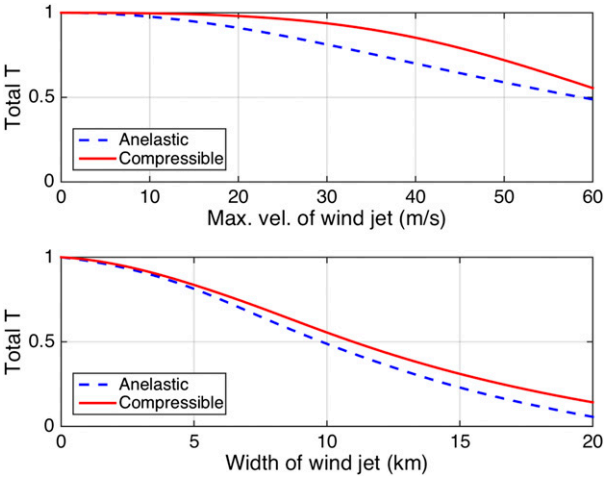

FIG. 6. Total transmission T in wind jets of different (top) maximum velocities and (bottom) widths.

the anelastic case and is identical to the top panel of Fig. 4 in BED. Initially, there are 112 waves that propagate from the sea surface up to around 70 km. They encounter the wind jet and m^2/K_0^2 decreases when some waves become evanescent when m^2/K_0^2 drops below zero. Between 87 and 97 km, there is a local maximum, when waves resume propagating until they encounter the second local minimum and maximum between 97 and 140 km. Finally, above 140 km, all waves become propagating again.

In right panel of Fig. 3, for the compressible case, there are 143 initially propagating waves with two local minima and maxima in m^2/K_0^2 between 70–100 and 100–130 km. However, the curves show a dramatically different pattern: the first local minimum is amplified so that it almost has the same minimum as the second one; the positive maximum is also amplified, while its peak moves up from 95 km in the left panel to 100 km. The overall pattern turns out to be almost symmetric about the central axis of the wind jet in the compressible case. This is not fortuitous: the sum of the two asymmetric terms $2(g/U^2)(D_z/D)$ and $-SD_z/D$ that are included in the compressible case leads to an asymmetric contribution that almost cancels the asymmetry in the anelastic case: $SU_z/U \approx -SD_z/D$ and $(g/U^2)(D_z/D) \approx -SD_z/D$. Combining (12), (1), (11), and (15), we obtain $c/c_s = O(1)$ and $H/H_s = O(1)$. This cancellation is because the tsunami phase speed and the sound speed in the atmosphere have the same order of magnitude, as do the depth of sea and the atmospheric density scale height. This symmetry property affects the height of turning points as well as the distribution of the propagating and evanescent regions.

The left panels of Fig. 4 show the normalized vertical velocity w/W_0 for the total, upgoing, and downgoing waves in the anelastic case. First, initially upgoing waves generated by the tsunami propagate up to around 70 km until some waves become evanescent in the region between 70 and 93 km. This corresponds to the first local minimum in the left panel of Fig. 3 when m^2/K_0^2 for some waves drops below zero. When waves reach their turning points at $m^2/K_0^2 = 0$, some energy is transmitted and the rest is reflected. The evanescent region between 100 and 130 km corresponds to the second local minimum in the left panel of Fig. 3. Finally, above 130 km, all waves are propagating and upgoing.

The right panels of Fig. 4 show w/W_0 for the total, upgoing, and downgoing waves in the compressible case.

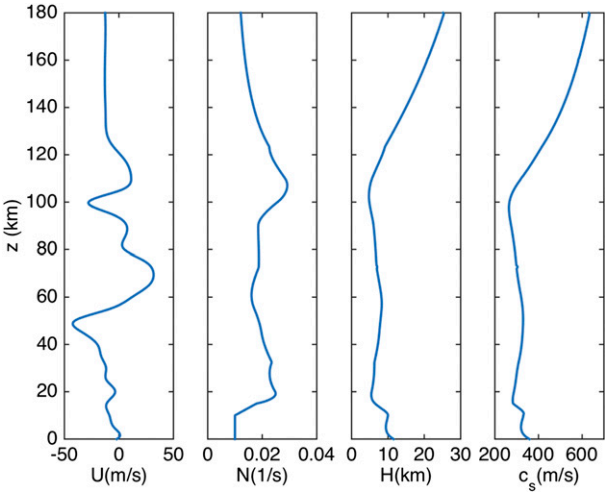

FIG. 7. Atmospheric profiles in the 2004 Sumatra tsunami case.

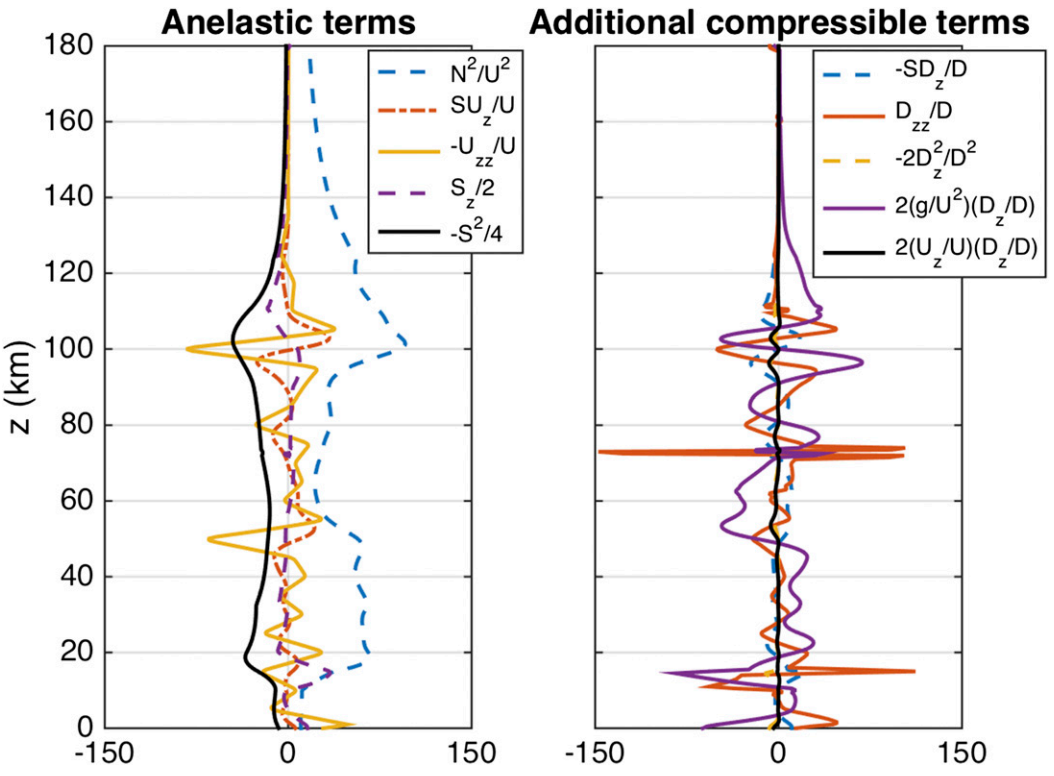

FIG. 8. Terms in m^2/K_0^2 in the 2004 Sumatra tsunami case.

There are four clear turning points and two evanescent regions at 75–98 and 102–125 km corresponding to the two local minima in the right panel of Fig. 3. Comparing the left and right columns of Fig. 4, we see that compressibility has a clear impact on the height of turning points and the distribution of the propagating and evanescent regions.

Figure 5 shows the transmission and reflection coefficients calculated from (24) and (25) for each initially propagating wave, as well as the tsunami vertical velocity $|\tilde{W}(k)|$ (not to scale). The result shows that $T(k)$ is enhanced by approximately 5% for small $|k|$ and 24% for large $|k|$, and $R(k)$ is diminished by approximately 6% for small $|k|$ and 8% for large $|k|$.

The total transmission coefficient for all Fourier components is defined as

$$\text{Total } T = \frac{\int A(k, z_{\max})^2 m(k, z_{\max})\, dk}{\int A(k,0)^2 m(k,0)\, dk}. \qquad (29)$$

Total T depends on the physical geometry of the wind jet (amplitude plus width). The dependence is illustrated in Fig. 6 showing that the faster or wider the wind, the smaller the total transmission. More importantly, both figures show that compressibility enhances the total transmission significantly.

c. *Case 3: 2004 Sumatra tsunami*

We investigate the wave propagation through the realistic atmospheric profile in the 2004 Sumatra tsunami as in BED. Air density is obtained from NRLMSISE-00, the empirical atmosphere model as described in Picone et al. (2002), where N is artificially replaced by a representative value of $N = 0.01\,\text{s}^{-1}$ below 15 km owing to the large oscillation of the calculated N in the lower troposphere from the model output. Wind velocity is obtained from HWM07, the latest version of the empirical model of the Earth's horizontal wind fields as described in Drob et al. (2008). All data are obtained for the center of the Indian Ocean at 0°, 85°E at 0300 UTC 26 December 2004 and the sound speed is calculated from the obtained data by combining (14) and (15). Figure 7 shows the parameters including horizontal background velocity U, buoyancy frequency N, density scale height H, and the speed of sound c_s.

The left panel of Fig. 8 shows the anelastic terms in m^2/K_0^2 corresponding to BED's Fig. 12. We see that the

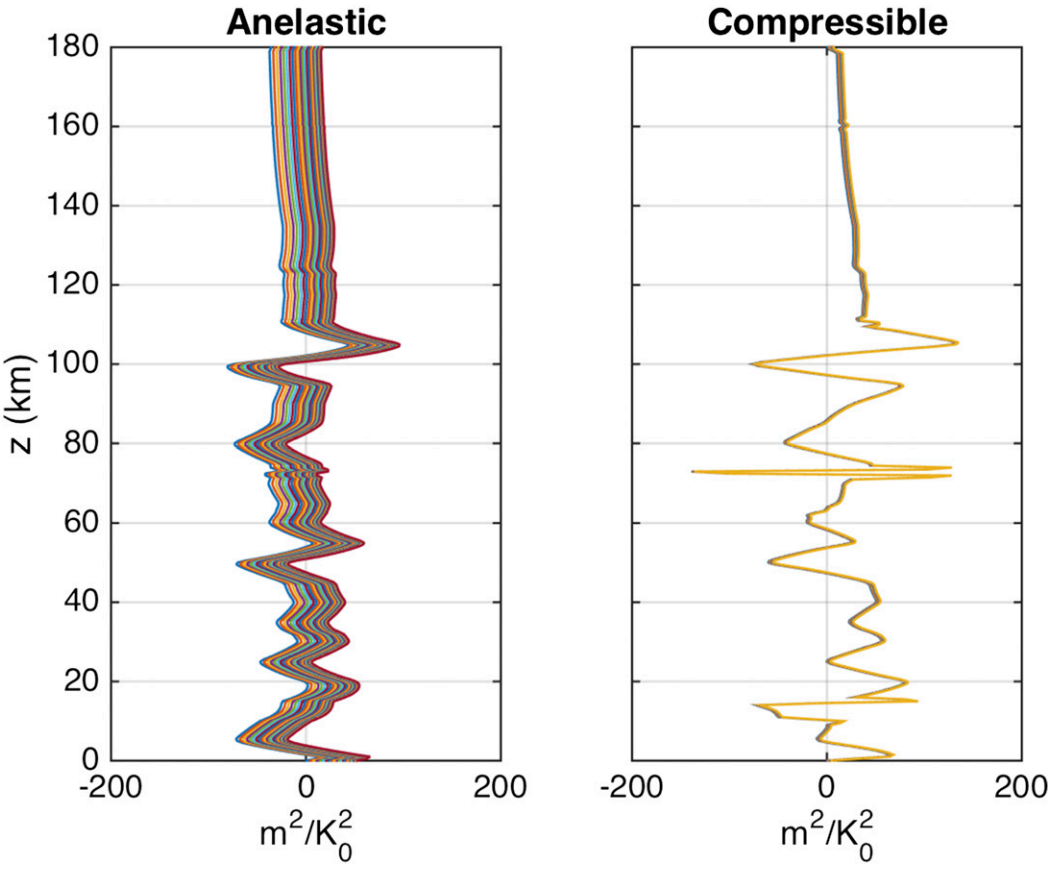

FIG. 9. Profiles of m^2/K_0^2 for every 10 initially propagating waves in the 2004 Sumatra tsunami case.

largest positive term at most altitudes is N^2/U^2, while the term $-U_{zz}/U$ stands out with the largest negative value at 50 and 100 km. The right panel of Fig. 8 shows the additional compressible terms except for k^2D^2 in m^2/K_0^2. The term D_{zz}/D has the maximum variability; to be specific, it has a significant positive value at 16 km and a dramatic fluctuation between positive and negative at 72–75 km. The term $2(g/U^2)(D_z/D)$ has a nonnegligible negative value at the sea surface, whose negative effect on m^2 at $z = 0$ will drive more waves into evanescence, thus result in fewer initially propagating waves. All five additional compressible terms are negligible above 140 km.

Figure 9 shows m^2/K_0^2 for every 10 initially propagating waves in the tsunami case. There are 276 and 97 initially propagating waves in the anelastic and compressible cases, respectively. The left panel for the anelastic case is identical to the top panel of BED's Fig. 4. Comparing the two panels, we find the fluctuation of m^2/K_0^2 in the compressible case is much larger than that in the anelastic case. There are fewer initially propagating waves and no turning points between 18 and 48 km and above 102 km in the compressible case.

The left panels of Fig. 10 shows w/W_0 for the total, upgoing, and downgoing waves in the anelastic case, while the right panels represent the compressible case, respectively. The anelastic results are identical to those of Fig. 10 in BED, while the compressible results show both the upgoing and downgoing waves are weaker. That attributes to the additional compressible term $2(g/U^2)(D_z/D)$ whose negative effect on m^2 at $z = 0$ leads to fewer initially propagating waves. Combining the anelastic and the compressible results, we conclude that compressibility has a nonnegligible effect on the wave transmission and reflection and the number of initially propagating waves.

Figure 11 shows the transmission and reflection coefficients $T(k)$ and $R(k)$ with the tsunami vertical velocity $|\tilde{W}(k)|$ on the bottom (not to scale) for all initially propagating waves in the anelastic and compressible case, respectively. The compressible results show a noticeable difference: there is a clear cutoff wavenumber at $k = -2.6K_0$ indicating waves with $k < -2.6K_0$ are not propagating anymore; there is an evident decrease of $R(k)$ and an increase of $T(k)$ for waves with $k > -2.55K_0$, especially for waves with smaller $|k|$.

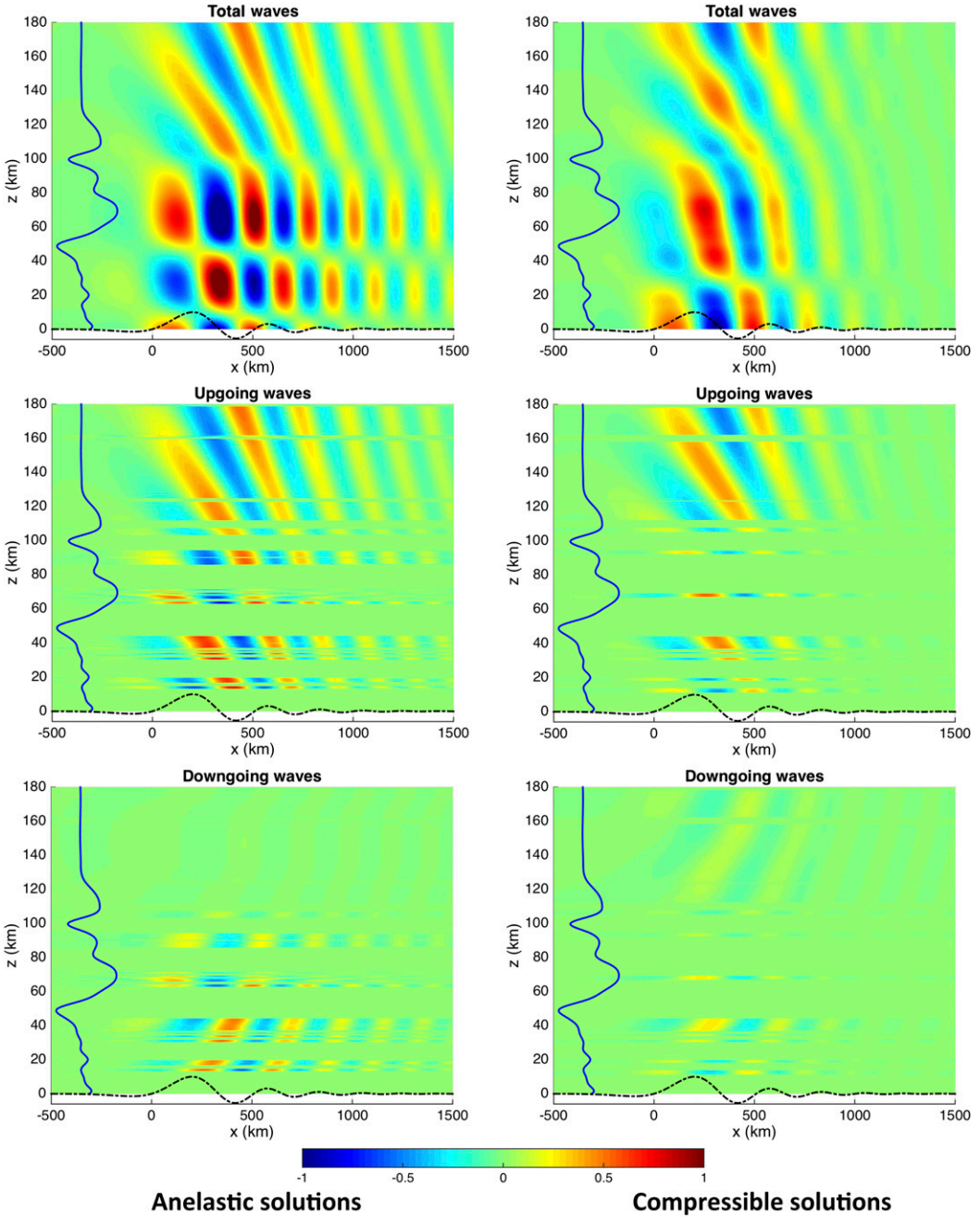

FIG. 10. Cross sections of w/W_0 for the (top) total, (middle) upgoing, and (bottom) downgoing waves with $h(x)$ and $U(z)$ (not to scale) in the (left) anelastic and (right) compressible cases.

4. Conclusions

We expect compressibility to be important since the Mach number U/c_s is close to 1 in the tsunami reference frame. We investigate the five additional compressible terms in the expression of m^2 that include the Doppler effect. They have large variations that are comparable to the anelastic terms, indicating a nonnegligible effect on the vertical structure.

In the idealized wind jet case, we find compressibility affects the number and height of turning points as well as the distribution of evanescent regions. A symmetric distribution about the central axis of the wind jet is observed in the compressible case. By calculating the transmission and reflection coefficients for each Fourier component through the whole atmosphere, we find that in general compressibility

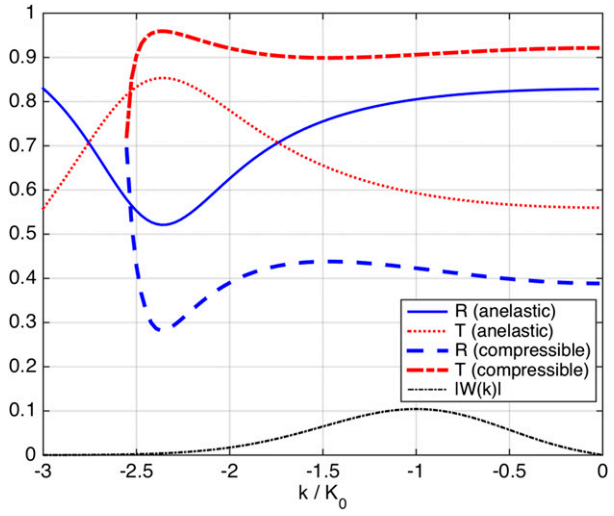

FIG. 11. $T(k)$, $R(k)$, and $|\tilde{W}(k)|$ (not to scale) in the 2004 Sumatra tsunami case.

enhances the transmission coefficient, especially for large $|k|$. For the wind profile that we use in case 2, $T(k)$ is enhanced by approximately 5% for small $|k|$ and by 24% for large $|k|$. We also calculate the total transmission for all Fourier components. By varying the maximum velocity or the width of the wind jet, we find that a faster or wider wind jet will drive more waves into evanescence. Since we manually select the exponentially decaying solution as $z \to \infty$ in the evanescent regions, the conclusion of reduced total transmission is obvious. In the 2004 Sumatra tsunami case, weaker reflected waves and enhanced total transmission are observed in the compressible case. Specifically, transmission is reduced for large $|k|$ and enhanced for small $|k|$.

Wei et al. (2015) presents an idealized theoretical and numerical study of two-dimensional tsunami-generated acoustic–gravity waves in a two-layer atmosphere. They include compressibility by using a fully compressible formulation and include time by computing the detailed evolution of wave propagation. They observe significant partial reflection of waves in the nonuniformly stratified atmosphere and find that the acoustic signal is the first and strongest to arrive at the ionosphere. Compared to Wei et al. (2015), our study considers stationary solutions and includes the realistic atmospheric data (N, H, c_s) as well as a height-varying horizontal background wind.

Acknowledgments. This work was supported by ONR Award N00014-13-1-0347.

APPENDIX

Derivation of (13)

We start from the linearized governing equations [(5)–(8)], where there are four equations and four unknowns (u_1, w_1, p_1, ρ_1). We eliminate u_1 and ρ_1, yielding

$$(A + B\partial_z)p_1 + (C + D\partial_z)w_1 = 0 \quad \text{and} \tag{A1}$$

$$Ep_1 + (F + G\partial_z)w_1 = 0, \tag{A2}$$

where $A = -ik/U$, $B = -ikU/g$, $C = \rho_{0z} - \rho_0 U_z/U + \rho_0 k^2 U^2/g$, $D = \rho_0$, $E = (U - c^2/U)ik$, $F = -\rho_0 g - c^2\rho_0 U_z/U$, and $G = c^2\rho$.

We combine (A1) with (A2) and obtain a second-order ODE in w_1:

$$w_{1zz}(BEG) + w_{1z}(AEG + BEF - BE'G + BEG' - DE^2) + w_1(AEF - BE'F + BEF' - CE^2) = 0. \tag{A3}$$

Substituting the coefficients A, B, C, D, E, and F, we derive

$$w_{1zz}(c^4 - c^2U^2) + w_{1z}\left(c^4\frac{\rho_{0z}}{\rho_0} + 2c^2UU_z - c^2U^2\frac{\rho_{0z}}{\rho_0}\right) + w_1\left[c^4\left(-\frac{g}{U}\frac{\rho_{0z}}{\rho_0} - k^2 - \frac{U_{zz}}{U} - \frac{U_z}{U}\frac{\rho_{0z}}{\rho_0}\right) + c^2\left(-\frac{g^2}{U^2} - 2g\frac{U_z}{U} - 2U_z^2 + UU_z\frac{\rho_{0z}}{\rho_0} + UU_{zz} + 2U^2k^2 + g\frac{\rho_{0z}}{\rho_0}\right) + (g^2 - U^4k^2)\right] = 0. \tag{A4}$$

We observe the ratio of the coefficient of w_{1z} to that of w_1 satisfies

$$\frac{\rho_{0z}/\rho_0 + 2UU_z/c^2 - (U^2/c^2)(\rho_{0z}/\rho_0)}{1 - U^2/c^2} = \frac{\rho_{0z}}{\rho_0} + \frac{2UU_z/c^2}{1 - U^2/c^2} = \frac{d}{dz}\left[\log\rho_0 - \log\left(1 - \frac{U^2}{c^2}\right)\right]. \tag{A5}$$

To eliminate the first-order derivative term in (A4), we perform the change of variable given in (10):

$$w_{zz}+w\left[-\frac{g}{U^2}\frac{\rho_{0z}}{\rho_0}-\frac{g^2}{U^2c^2}-\frac{\rho_{0z}}{\rho_0}\frac{U_z}{U}-\frac{U_{zz}}{U}-\frac{1}{2}\frac{\rho_{0zz}}{\rho_0}+\frac{1}{4}\left(\frac{\rho_{0z}}{\rho_0}\right)^2-k^2D^2+\frac{\rho_{0z}}{\rho_0}\frac{D_z}{D}+\frac{D_{zz}}{D}-\frac{2D_z^2}{D^2}+\frac{2g}{U^2}\frac{D_z}{D}+\frac{2U_z}{U}\frac{D_z}{D}\right]=0, \tag{A6}$$

which yields (13).

REFERENCES

Artru, J., V. Ducic, H. Kanamori, P. Lognonné, and M. Murakami, 2005: Ionospheric detection of gravity waves induced by tsunamis. *Geophys. J. Int.*, **160**, 840–848, doi:10.1111/j.1365-246X.2005.02552.x.

Bretherton, F. P., and C. J. R. Garrett, 1968: Wavetrains in inhomogeneous moving media. *Proc. Roy. Soc. London*, **302**, 529–554, doi:10.1098/rspa.1968.0034.

Broutman, D., S. D. Eckermann, and D. P. Drob, 2014: The partial reflection of tsunami-generated gravity waves. *J. Atmos. Sci.*, **71**, 3416–3426, doi:10.1175/JAS-D-13-0309.1.

Coïsson, P., P. Lognonné, D. Walwer, and L. M. Rolland, 2015: First tsunami gravity wave detection in ionospheric radio occultation data. *Earth Space Sci.*, **2**, 125–133, doi:10.1002/2014EA000054.

Ding, F., W. Wan, and H. Yuan, 2003: The influence of background winds and attenuation on the propagation of atmospheric gravity waves. *J. Atmos. Sol.-Terr. Phys.*, **65**, 857–869, doi:10.1016/S1364-6826(03)00090-7.

Drob, D. P., and Coauthors, 2008: An empirical model of the Earth's horizontal wind fields: HWM07. *J. Geophys. Res.*, **113**, A12304, doi:10.1029/2008JA013668.

Fröman, N., and P. O. Fröman, 2002: *Physical Problems Solved by the Phase-Integral Method*. Cambridge University Press, 232 pp.

Galvan, D. A., A. Komjathy, M. P. Hickey, and A. J. Mannucci, 2011: The 2009 Samoa and 2010 Chile tsunamis as observed in the ionosphere using GPS total electron content. *J. Geophys. Res.*, **116**, A06318, doi:10.1029/2010JA016204.

——, ——, ——, P. Stephens, J. Snively, Y. Tony Song, M. D. Butala, and A. J. Mannucci, 2012: Ionospheric signatures of Tohoku-Oki tsunami of March 11, 2011: Model comparisons near the epicenter. *Radio Sci.*, **47**, RS4003, doi:10.1029/2012RS005023.

Hickey, M. P., G. Schubert, and R. L. Walterscheid, 2009: Propagation of tsunami-driven gravity waves into the thermosphere and ionosphere. *J. Geophys. Res.*, **114**, A08304, doi:10.1029/2009JA014105.

——, R. L. Walterscheid, and G. Schubert, 2010: Wave mean flow interactions in the thermosphere induced by a major tsunami. *J. Geophys. Res.*, **115**, A09309, doi:10.1029/2009JA014927.

Hines, C. O., 1960: Internal atmospheric gravity waves at ionospheric heights. *Can. J. Phys.*, **38**, 1441–1481, doi:10.1139/p60-150.

Lighthill, M. J., 2001: *Waves in Fluids*. 6th ed. Cambridge University Press, 524 pp.

Liu, J.-Y., Y.-B. Tsai, K.-F. Ma, Y.-I. Chen, H.-F. Tsai, C.-H. Lin, M. Kamogawa, and C.-P. Lee, 2006: Ionospheric GPS total electron content (TEC) disturbances triggered by the 26 December 2004 Indian Ocean tsunami. *J. Geophys. Res.*, **111**, A05303, doi:10.1029/2005JA011200.

Mai, C.-L., and J.-F. Kiang, 2009: Modeling of ionospheric perturbation by 2004 Sumatra tsunami. *Radio Sci.*, **44**, RS3011, doi:10.1029/2008RS004060.

Occhipinti, G., P. Lognonné, E. A. Kherani, and H. Hébert, 2006: Three-dimensional waveform modeling of ionospheric signature induced by the 2004 Sumatra tsunami. *Geophys. Res. Lett.*, **33**, L20104, doi:10.1029/2006GL026865.

——, E. A. Kherani, and P. Lognonn, 2008: Geomagnetic dependence of ionospheric disturbances induced by tsunamigenic internal gravity waves. *Geophys. J. Int.*, **173**, 753–765, doi:10.1111/j.1365-246X.2008.03760.x.

——, P. Coïsson, J. J. Makela, S. Allgeyer, A. Kherani, H. Hebert, and P. Lognonné, 2011: Three-dimensional numerical modeling of tsunami-related internal gravity waves in the Hawaiian atmosphere. *Earth Planets Space*, **63**, 847–851, doi:10.5047/eps.2011.06.051.

Peltier, W. R., and C. O. Hines, 1976: On the possible detection of tsunamis by a monitoring of the ionosphere. *J. Geophys. Res.*, **81**, 1995–2000, doi:10.1029/JC081i012p01995.

Picone, J. M., A. E. Hedin, D. P. Drob, and A. C. Aikin, 2002: NRLMSISE-00 empirical model of the atmosphere: Statistical comparisons and scientific issues. *J. Geophys. Res.*, **107**, 1468, doi:10.1029/2002JA009430.

Rolland, L. M., G. Occhipinti, P. Lognonné, and A. Loevenbruck, 2010: Ionospheric gravity waves detected offshore Hawaii after tsunamis. *Geophys. Res. Lett.*, **37**, L17101, doi:10.1029/2010GL044479.

Smith, R. B., 1979: The influence of mountains on the atmosphere. *Advances in Geophysics*, Vol. 21, Elsevier, 87–230, doi:10.1016/S0065-2687(08)60262-9.

Wei, C., O. Bühler, and E. G. Tabak, 2015: Evolution of tsunami-induced internal acoustic–gravity waves. *J. Atmos. Sci.*, **72**, 2303–2317, doi:10.1175/JAS-D-14-0179.1.